Proceedings of the
Annual Stability Conference
Structural Stability Research Council
St. Louis, Missouri, April 2-5, 2019

Seismic performance of corrugated double-skin composite shear walls with different aspect ratios

Qiuhong Zhao[1], Yikang Li[2], Ying Tian[3]

Abstract
Corrugated double-skin composite shear (Co-DSC) walls consist of concrete filled steel tubes and a pair of corrugated steel faceplates connected by tie bolts with concrete infill. Three specimens with different shear-span ratios and one specimen with reinforcing sheaths at the bottom of steel tubes were tested under axial and cyclic lateral load. Failure pattern and cyclic behavior were presented and analyzed. Squat Co-DSC wall yielded by diagonal section of corrugated faceplate yielding, and failed by steel tube fracture, corrugated faceplate buckling, infilled concrete crushing and cracking. Slender corrugated DSCS walls yielded by steel tube yielding, and failed by steel tube fracture, steel faceplate buckled throughout wall base, and infilled concrete crushing. The strength, stiffness, and deformation capacities of squat Co-DSC wall were higher than that of slender Co-DSC walls, while the ductility and energy dissipation capacity were the opposite. Test results revealed that the proposed bottom reinforcing sheaths could improve deformation capacity of the slender wall, meanwhile the base shear was not increased. Stronger boundary columns are recommended to be used in the corrugated DSCS walls to improve the seismic performance. Finite element (FE) push-over analyzes were conducted, and were in good agreement with the test results. Primary parameters, including aspect ratio, axial load ratio, and ratio of tie bolt spacing to faceplate thickness, that influencing the overall behavior of Co-DSC walls were analyzed.

1. Introduction

Double-skin composite (DSC) wall, consisting of two exterior steel faceplates connected to each other by connectors and infilled with plain concrete, is an effective axial and lateral load resisting system. DSC wall was first proposed by Hitachi Ltd. for coastal buildings to resist the impact load caused by wave and iceberg shocking (Stephens and Zimmerman 1990) and prompted further studies (Link and Elwi 1995; Ozaki et al. 2004). More DSC walls were then proposed for use in tunnels and safety-related nuclear facilities, with different types of connectors such as headed studs (Shanmugam et al. 2002), Bi-Steel^{TM} connectors (Mckinley and Boswell 2002; Clubley et al. 2003), and J-hook connectors (Liew and Sohel 2009; Huang and Liew 2016).

[1] Professor, Tianjin University, <qzhao@tju.edu.cn>
[2] Ph.D. Candidate, Tianjin University, <liyikang@tju.edu.cn>
[3] Associate Professor, University of Nevada, <ying.tian@unlv.edu>

Recently, DSC walls have also been used as a lateral-load resisting system in building structures, usually with concrete-filled steel tubes as the boundary elements and faceplates connected by tie bolts (Ji et al. 2013; Rassouli et al. 2016) or batten plates (Nie et al. 2013). Research has proven that the DSC walls present high axial and lateral strengths, lateral stiffness, ductility, and energy dissipation capacity. Moreover, the use of steel faceplates improves construction efficiency because they function as stay-in-place formwork for concrete casting.

Research showed that the seismic performance of DSC walls, such as hysteretic response and failure modes, are strongly affected by axial load ratio, wall aspect ratio, and structural details (Qian et al. 2012; Nie et al. 2013; Epackachi et al. 2015). The behavior of DSC walls with high aspect ratios is governed by flexure, and the ultimate failure is generally caused by steel tube fracture; however, the behavior of DSC walls with low aspect ratios is governed by shear, and the ultimate failure is normally caused by steel faceplate buckling and concrete crushing (Nie et al. 2013; Ji et al. 2017; Seo et al. 2016). For flexure-controlled DSC walls, reinforcing the bottom of steel tubes by welding steel plates could prevent the buckling and fracture there, but the steel tube right above the reinforced region buckled and fractured later instead (Cao et al. 2013). Furthermore, the welded steel plates also participated in lateral resisting, thus increasing the wall base shear and demand on foundations. Therefore, a reinforcing measure was proposed in this research, which could prevent the bottom of steel tubes from early buckling, yet did not participate in lateral resisting.

Faceplates of the DSC walls in previous research were usually flat and thus prone to out-of-plane deformation under large lateral pressure from the wet concrete during construction, especially if the DSC walls are used in high-rise buildings where the walls are relatively thick (Ovarlez and Roussel 2006). In addition, the ratio of connector spacing to plate thickness was suggested to be limited within 37 (Wright 1995) for flat faceplates to prevent local buckling, resulting in the use of a large number of connectors. Corrugated faceplates offer a better choice. The much higher out-of-plane bending stiffness prevent buckling during concrete casting and help reduce the number of connectors, thereby leading to a much more efficient construction of DSC walls.

Wright and Gallocher (1995) proposed a type of DSC wall panel with cold-formed profiled steel sheeting faceplates. Research were conducted on single panels without boundary columns under axial load and in-plane shear. The panels provided high shear resistance if adequate connections were ensured at the four-edges (Hossain and Wright 2004). Elastic buckling of the profiled steel sheeting could be prevented if enough fasteners were provided at the steel-concrete interface (Rafiei et al. 2015; Hossain et al. 2016). However, the panels were designed as shear panels only without boundary columns, while research on DSC walls with flat faceplates has revealed that boundary columns contributed to the deformation and energy dissipation capacity of the system significantly, especially in high-rise buildings (Qian et al. 2012; Ji et al. 2013). In addition, using hot-rolled steel would increase the system ductility further. Therefore, more adaptations are needed to apply DSC wall with corrugated faceplates in mid- to high-rise buildings.

This paper presents a new type of DSC shear wall system, namely corrugated double-skin composite (Co-DSC) walls, to be used in mid- to high-rise buildings in seismic zones. As shown in Fig. 1, the proposed Co-DSC wall system consists of corrugated double steel faceplates connected by tie bolts, infilled plain concrete, and concrete-filled steel tube boundary columns.

The corrugated steel plates and steel tubes are fabricated by hot-rolled steel to meet the ductility requirements of seismic design. Cyclic tests were carried out on three specimens with different aspect ratios and one additional specimen with reinforcing sheaths at the bottom of concrete-filled steel tubes. The seismic performance of the test specimens was evaluated in terms of damage and failure pattern, hysteretic response, strength and stiffness characteristics, deformation property, and energy dissipation capacity. Finite element (FE) analyzes were conducted after the test, and have been proven that can reasonably predict the load-displacement behavior of the test specimens. The effects on system lateral load-displacement relationship of aspect ratio, axial load ratio, and ratio of tie bolt spacing to faceplate thickness were considered.

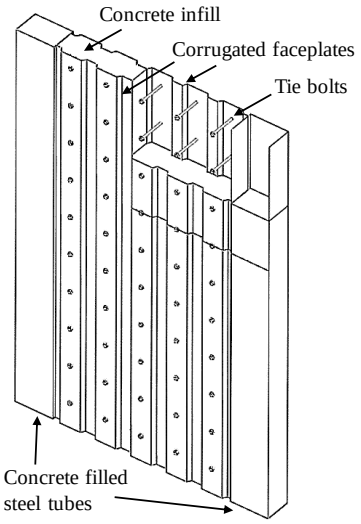

Figure 1: Schematic of proposed Co-DSC wall system

2. Experimental Program

2.1 Specimen Design

Four specimens, designated as DCW1, DCW2, DCW3 and DCW3-R, were tested at a 1/3 scale. Fig. 2 shows specimen geometry and structural details. Each specimen contained a concrete-filled double corrugated steel faceplates web, with a width of 700 mm and a thickness of 70~100 mm, and two 150 × 100 mm rectangular concrete-filled steel tube columns. The overall cross-section dimension of the specimens was identically 1000 mm wide and 100 mm thick. The steel tubes were made of 3.5-mm thick hot-rolled seamless steel. The two corrugated steel faceplates were fabricated from 2.7-mm thick flat hot-rolled steel plates and fixed to each other by 8-mm diameter (D8) high strength bolts. The typical ratio of bolt spacing to plate thickness κ was 56. The effective height of specimens DCW1, DCW2, and DCW3, measured from lateral loading position to wall bottom, was 1000, 1500, and 2000 mm, leading to an aspect ratio λ of 1.0, 1.5, and 2.0, respectively. Specimen DCW3-R was identical to DCW3 except that reinforcing sheaths were attached to the bottom of each steel tube with an aim to constrain its buckling. Each reinforcing sheath was fabricated by welding three pieces of 5.7-mm thick steel plates together and connected to the steel tube by D8 high strength bolts.

The loading and foundation beams were both concrete-filled steel boxes. An opening was cut on the top plate of the foundation beam as well as the bottom plate of the loading beam to accommodate the specimen, which was securely welded to the bottom plate of the foundation

beam and top plate of the loading beam. Longitudinal, transverse and anchor bars with a diameter of 25 mm (D25) were erected inside the loading and foundation beams to anchor the specimen, and these beams were cast together with the specimen. Prior to testing, one side of the specimen was coated with whitewash painting to facilitate observing damage condition.

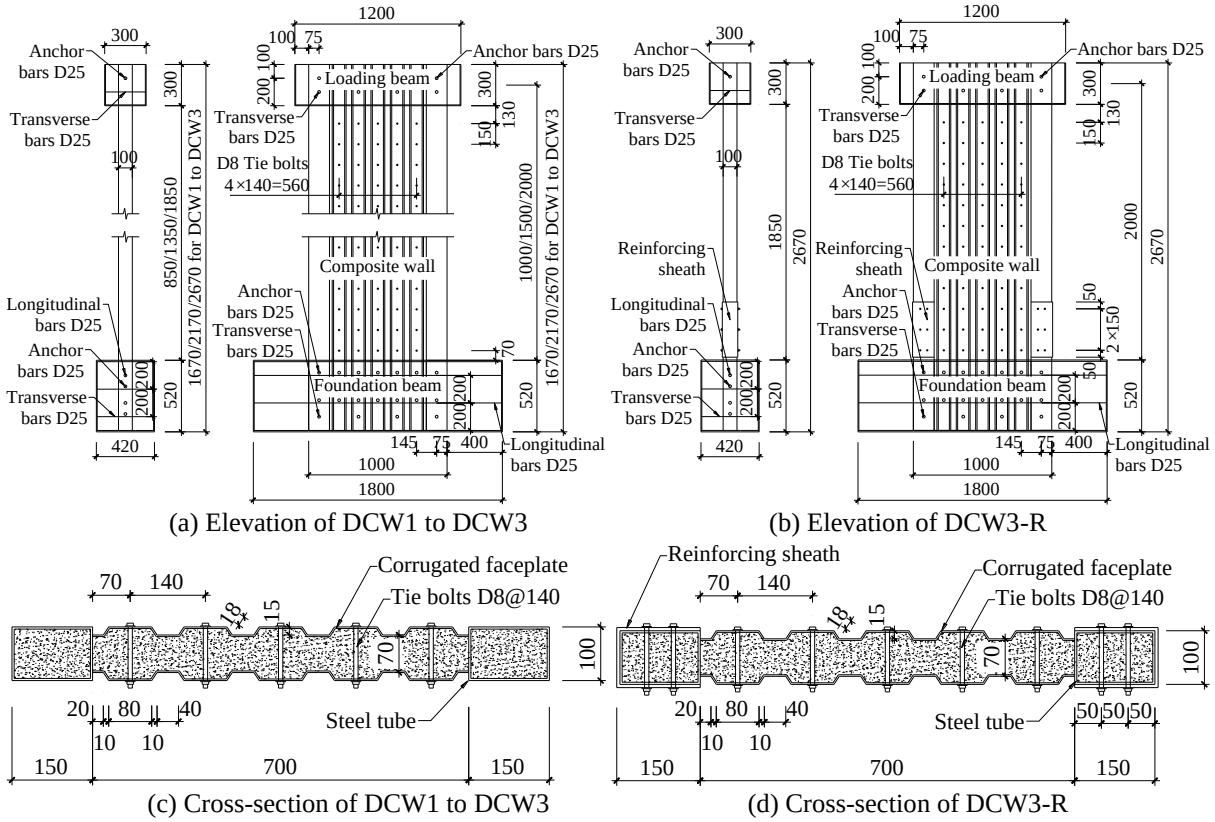

(a) Elevation of DCW1 to DCW3 (b) Elevation of DCW3-R

(c) Cross-section of DCW1 to DCW3 (d) Cross-section of DCW3-R

Figure 2: Geometric and structural details of specimens (dimension in mm)

2.2 Material Properties

The four specimens were poured with the same batch of concrete, with a compressive strength of 33.7 MPa based on testing results of three 100 mm cubes made of the same concrete used to construct the wall specimens. Concrete Young's modulus was determined from compressive material tests as 2.92×104 MPa. Coupons cut from the steel tubes and faceplates for fabricating the specimens were tested under monotonic tensile loading. Table 1 gives the measured yield strength, ultimate tensile strength, and Young's modulus. The high strength tie bolts had a nominal yield stress of 640 MPa and a nominal ultimate strength of 800 MPa.

Table 1: Material properties of steel components

Steel type	Thickness (mm)	Yield strength (MPa)	Tensile strength (MPa)	Young's modulus (MPa)
Faceplate	2.7	307	445	2.02×10^5
Tube	3.5	328	386	2.02×10^5
Reinforcing sheath	5.7	306	457	1.94×10^5

2.3 Test Setup and Loading Protocol

Fig. 3 shows the test setup used to apply axial and lateral loads on the specimens. The foundation beam was clamped to a strong floor by two steel beams and high strength fastening bolts, with two reaction blocks situated on both sides to further restrain it from horizontal movement. Downward axial load was applied by a hydraulic jack bearing against the beam of a rigid steel load frame through a rolling support. A steel spreader beam was used to distribute the axial load evenly to the specimen. Horizontal cyclic loading was applied at the mid-height of the loading beam by a hydraulic actuator fixed to a reaction wall. Both the horizontal actuator and the vertical jack had a loading capacity of 2000 kN. A pair of steel braces, one at the front side of the specimen and the other one at the back side, were fixed to the load frame to prevent the specimen from out-of-plane bending and twisting during the test.

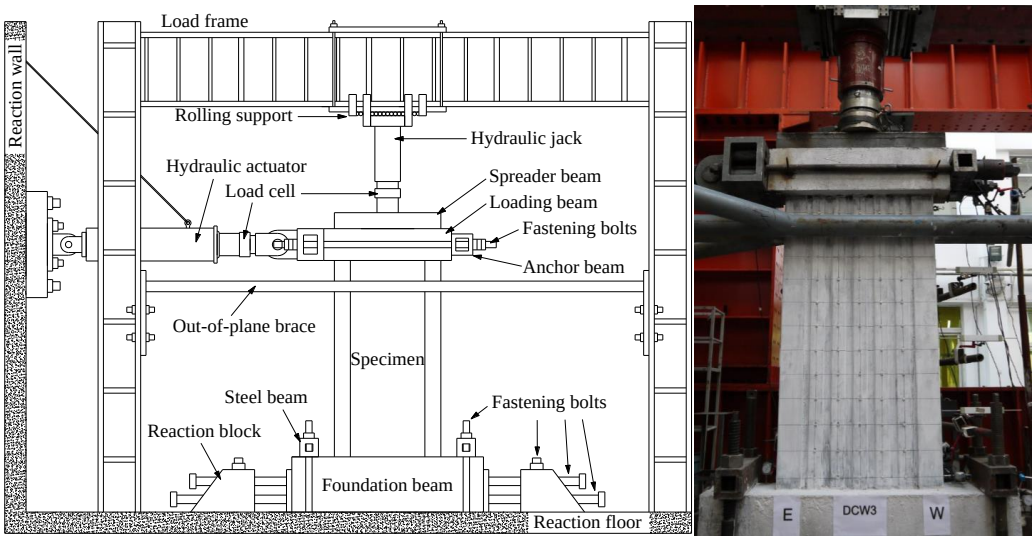

Figure 3: Test setup

The test of a specimen began with applying an axial load of N = 1100 kN, resulting in an axial force ratio of n = 0.21 evaluated based on Eq. 1. This axial load was maintained to be constant during the subsequently applied cyclic lateral loading.

$$n = \frac{N}{f_c A_c + f_{yp} A_p + f_{yt} A_t} \tag{1}$$

where f_c is the concrete compressive strength, A_c is the total cross-sectional area of concrete, f_{yp} is the yield strength of steel faceplates, A_p is the total cross-sectional area of two steel faceplates, f_{yt} is the yield strength of steel tubes, and A_t is the total cross-sectional area of two steel tubes.

Following the axial loading, displacement-controlled cyclic lateral loading was applied quasi-statically. Same lateral loading protocol was used for the specimens. Fig. 4 shows the target loading history in terms of drift ratio, defined as the ratio of horizontal displacement at the loading beam to wall effective height, and the loading cycle number at each drift level. In each loading cycle, a push was made first and followed by a pull, defined as positive (+) and negative loading (-), respectively. The initial loading of a specimen was used to simulate the elastic response. Target drift ratios of 0.125, 0.25, and 0.375%, with one loading cycle per drift level, were applied in this loading stage. During the subsequent loading stage, the specimen was

planned to experience 0.5, 0.75, 1, 1.5, 2, 2.5, and 3% drift ratios, with two loading cycles at each drift level. The testing was terminated as long as any of the following conditions occurred: (1) the lateral load at a target drift ratio declined to 85% of the peak lateral load, (2) the axial load could no longer be maintained due to specimen damage, and (3) the specimen was found to be severely damaged and thus unsuitable for further loading.

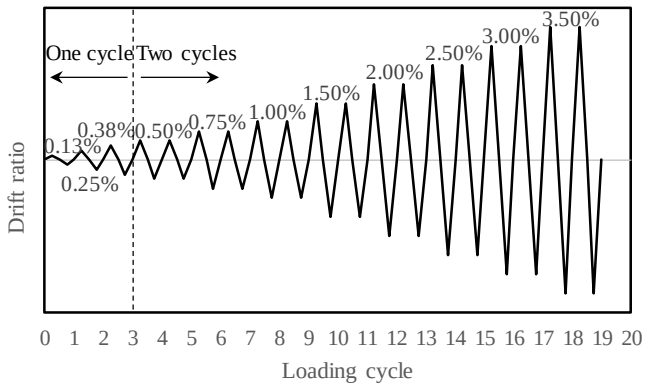

Figure 4: Lateral loading procedure

2.4 Instrumentation

The applied axial load was measured by a load cell placed between the hydraulic jack and the loading beam of specimen. The horizontal cyclic load was measured by a load cell installed with the actuator. A set of linear variable differential transformers (LVDTs) and dial gauges measured the horizontal or vertical displacement at various locations of a specimen. Fig. 5 shows the arrangement of LVDTs and dial gauges for testing specimen DCW3. LVDT L1, mounted at the mid-height of the loading beam, measured the horizontal displacement at wall top and was used to control cyclic loading in displacement mode. Four LVDTs (L2 through L5) and one dial gauge (L6) measured the lateral displacements at other locations along specimen height. Three dial gauges (L7, V1, and V2) were mounted on the foundation beam, measured its horizontal slippage and vertical uplift. Two LVDTs (V3 and V4) measured the axial deformation of the boundary columns. A pair of crossed LVDTs (D1 and D2) measured the wall diagonal deformation.

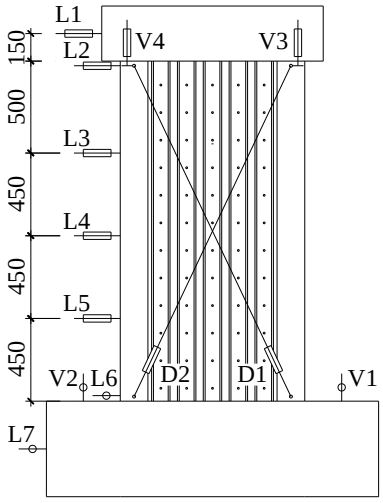

Figure 5: Instrumentation for specimen DCW3 (dimension in mm)

3. Test Results

3.1 Damage and Failure Patterns

All specimens experienced similar damage progress, including local buckling of steel tubes and faceplates, fracture of steel tubes, and concrete crushing at base of the wall. The damage progress can be characterized by three stages, including initial loading stage, damage developing stage, and failure stage, which can be summarized as follows. Note that the responses of specimen DCW3-R under negative and positive loading were slightly asymmetric for unknown reason, the average responses are described in following descriptions.

3.1.1 Initial loading stage

This stage began from the onset of testing up to the specimen reaching its yield load. The yield load is defined as the load causing a residual top displacement equal to 0.2% of wall effective height after unloading. Such yielding of specimens DCW1 to DCW3-R occurred at a drift ratio of 0.98, 0.54, 0.51, and 0.52%, respectively. No notable response was observed during the initial axial loading and the subsequent cyclic lateral loading up to the yield drift.

3.1.2 Damage developing stage

This stage started from the specimen yielding to reaching its peak load. For specimen DCW1, initial buckling occurred at the bottom of steel tubes and the lower corners of steel faceplates. As more loading cycles were applied, the buckling of steel tubes became obvious, the buckling of steel faceplates propagated from the bottom corners along the diagonal direction toward the center of wall web, indicating compression-shear damage pattern. The peak load of P_p = 1240 kN was reached at 2% drift. Specimens DCW2 and DCW3 presented similar observations at this stage, initial buckling occurred in a steel tube and became more obvious in the subsequent loading cycles. The peak load of P_p = 873 and 600 kN was reached at a drift around 1.5%, the buckling of steel faceplates propagated from the lower corners toward the center of wall web horizontally, indicating compression-flexure damage pattern. Different from other specimens, neither the steel tubes nor the faceplates experienced buckling prior to reaching 1.5% drift for DCW3-R, indicating that the reinforcing sheaths delayed steel tube buckling. The steel faceplates buckled at the lower corners around a drift of 1.5%. Because of the high compressive stress at the bottom of steel tubes, the reinforcing sheaths could not provide sufficient lateral constrain to the steel tubes, and consequently the steel tubes buckled due to the loss of restraint. The peak load of P_p = 610 kN was reached at 1.69% drift.

3.1.3 Failure stage

This stage started from the specimen reaching its peak load and continued to the test terminating. As more loading cycles were applied, the existing buckling became severe. The buckling at the bottom of the steel faceplates became diagonal for specimen DCW1, while the buckling at the bottom of the steel faceplates propagated throughout the wall base for specimens DCW2 to DCW3-R. All specimens finally failed by the bottom of steel tubes fracturing, accompanying with an outflow of crushed concrete powders. Ultimate drift is defined as the target drift corresponding to the lateral load declined to 85% of the peak lateral load. Such ultimate drift of specimens DCW1 to DCW3-R can be then determined as a drift of 2.65, 2.04, 1.96, and 1.81%, respectively.

After testing, the steel tubes and faceplate at the backside of all specimens were cut away to expose the concrete infilled into the steel tubes and the wall web. Final failure patterns of all specimens are shown in Fig. 6. Diagonal cracks of specimen DCW1 indicating concrete shear failure were densely distributed over the entire wall web and longitudinal concrete cracks existed in one of the steel tubes. Moreover, the buckling of steel tubes and steel faceplates resulted in the loss of constrain to the infilled concrete so that concrete crushing happened along the horizontal line where the steel tubes and steel faceplates severely buckled. For specimens DCW2 to DCW3-R, concrete crushed along the entire horizontal line where the steel tubes and steel faceplates severely buckled. Compared with specimen DCW1, less diagonal shear cracks were generated in the wall web especially at its upper portion where concrete was nearly intact.

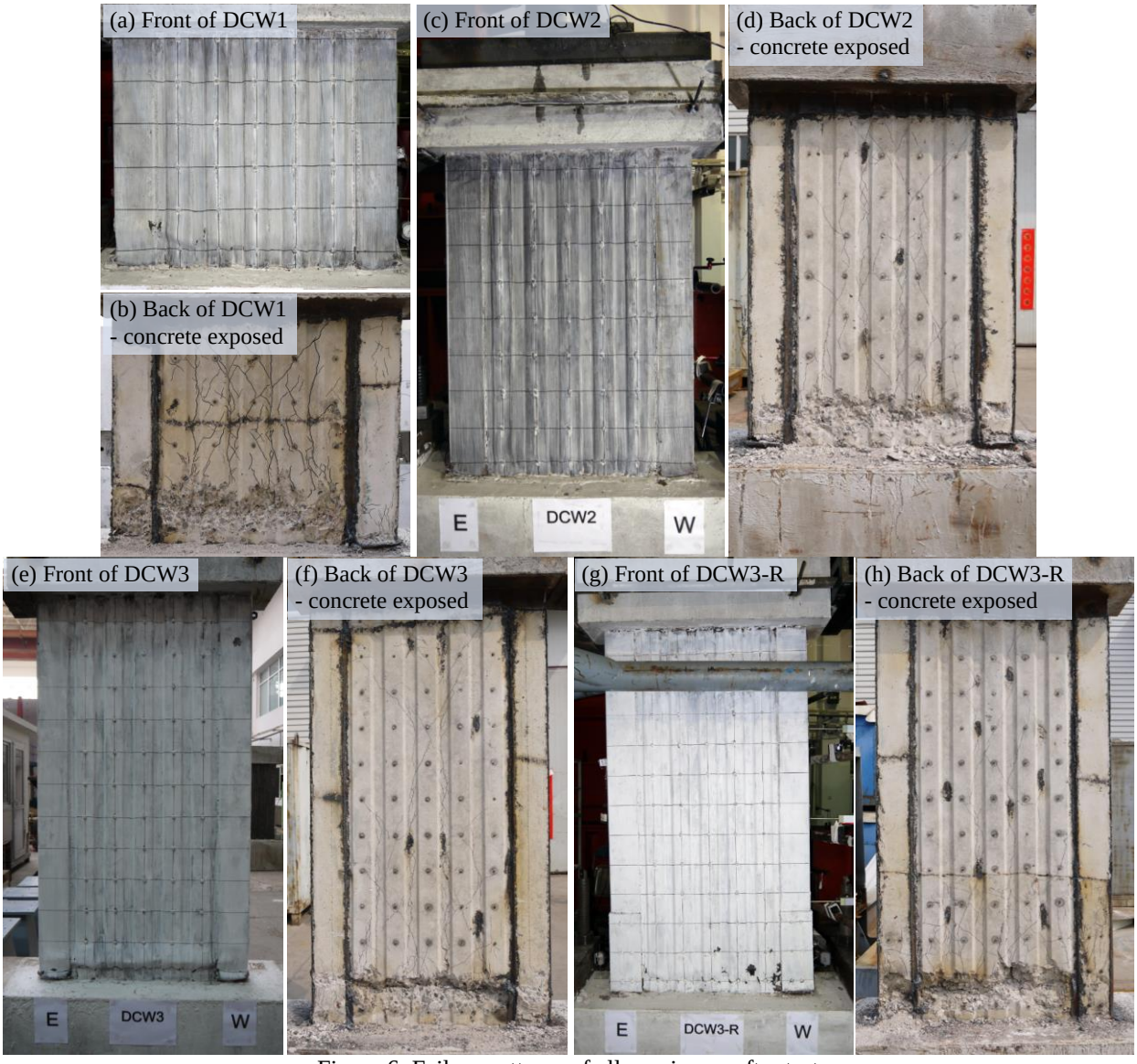

Figure 6: Failure patterns of all specimens after test

3.2 Lateral Load-Displacement Relationship

Fig. 7 shows the measured lateral load versus lateral displacement response for the test specimens. The hysteresis loops were relatively full without significant pinching, implying good energy dissipation capacity. The buckling of steel tube and faceplate and the fracture of steel tube are marked in the figures at the target lateral drifts when the testing was paused to observe damage. The overall yielding defined previously is also indicated in the figures. Table 2 summarizes the characteristic lateral loading responses of the specimens, including the initial stiffness K_0, overall yield load P_y, yield displacement d_y, yield drift ratio θ_y, peak load P_p, displacement at peak load d_p, drift ratio at peak load θ_p, ultimate displacement d_u, ultimate drift ratio θ_u, and ductility ratio μ.

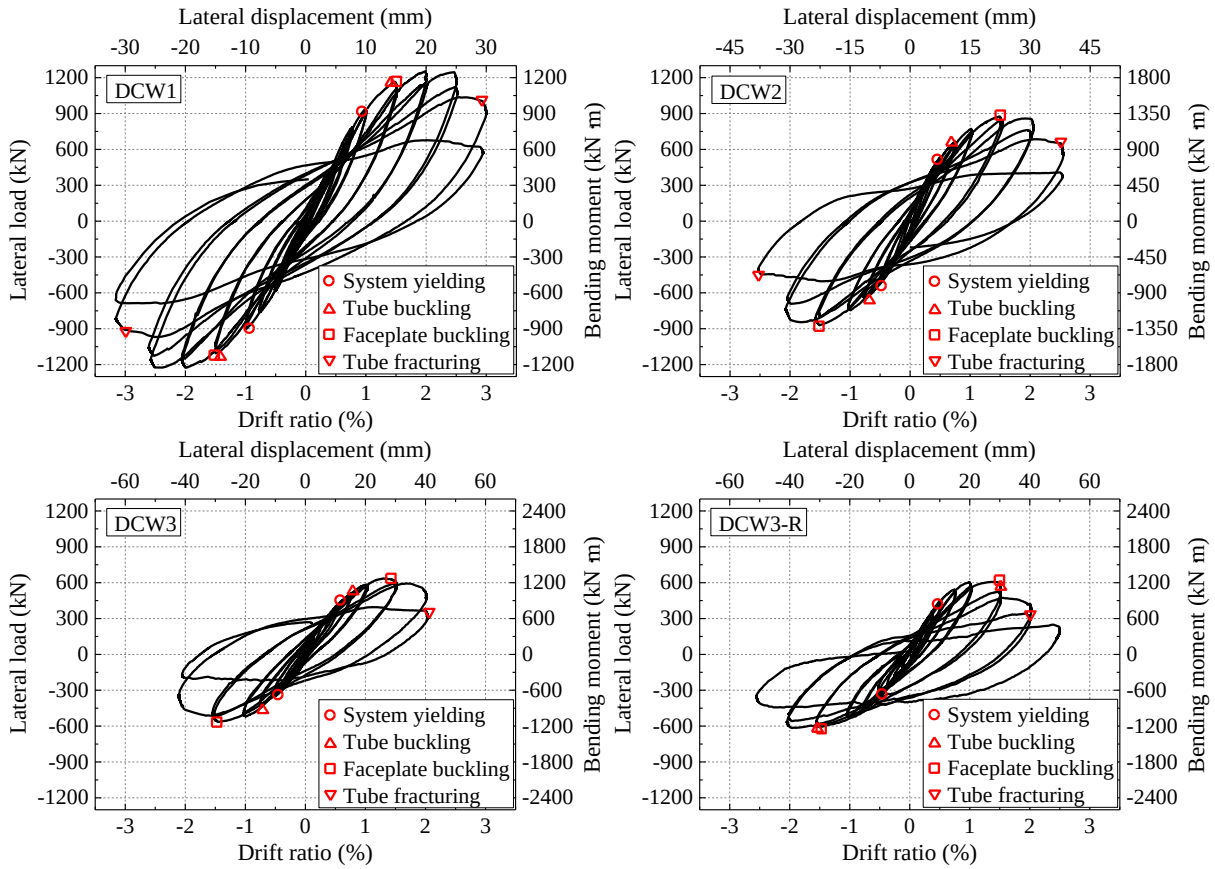

Figure 7: Hysteretic lateral load-drift responses

As seen in Fig. 7, the specimens behaved almost linearly before reaching the yield load P_y and there was negligible residual deformation upon unloading. DCW1 reached P_y at 1% drift, while the other specimens reached P_y approximately at 0.5% drift. The initial lateral stiffness K_0 and P_y decreased with the increased aspect ratio. Due to the lowest aspect ratio, the peak lateral load P_p achieved in specimen DCW1 was 1.42, 2.07, and 2.03 times that in DCW2, DCW3, and DCW3-R, respectively. DCW3 and DCW3-R had nearly identical P_p because the reinforcing sheaths in DCW3-R were attached to the steel tubes only by tie bolts and thus would not participate in resisting lateral loads. To examine the effect of aspect ratio on flexural capacity, the secondary vertical axis of Fig. 7 is used to indicate the bending moment resisted by a specimen. The average peak bending moment reached by DCW1, DCW2, DCW3, and DCW3-R was 1240, 1310, 1200, and 1220 kN m, respectively. The similar peak moments indicated that, despite the

more severe shear cracking suffered by specimen DCW1, aspect ratio had no impact on flexural strength when the wall specimens had the same cross-section.

Table 2: Characteristic lateral loading responses

Specimen	Loading direction	K_0 (kN/mm)	P_y (kN)	d_y (mm)	θ_y (%)	P_p (kN)	d_p (mm)	θ_p (%)	d_u (mm)	θ_u (%)	μ
DCW1	+	126	938	9.95	1.00	1254	20.0	2.00	26.9	2.69	2.69
	-	129	885	9.57	0.96	1226	20.0	2.00	26.1	2.61	2.72
	Avg.	128	912	9.76	0.98	1240	20.0	2.00	26.5	2.65	2.71
DCW2	+	106	555	8.25	0.55	875	22.5	1.50	30.9	2.06	3.75
	-	110	541	7.92	0.53	871	22.5	1.50	30.1	2.01	3.79
	Avg.	108	548	8.09	0.54	873	22.5	1.50	30.5	2.04	3.77
DCW3	+	58	422	10.9	0.55	634	26.6	1.33	40.0	2.00	3.64
	-	60	336	9.40	0.47	565	29.0	1.45	38.1	1.91	4.06
	Avg.	59	379	10.2	0.51	600	27.8	1.39	39.1	1.96	3.85
DCW3-R	+	62	437	9.74	0.49	607	28.1	1.40	31.2	1.56	3.18
	-	56	366	11.0	0.55	616	39.4	1.97	41.0	2.05	3.73
	Avg.	59	402	10.4	0.52	610	33.2	1.69	36.1	1.81	3.46

3.3 Deformation Properties

The ultimate deformation capacity is defined as the maximum top displacement or drift ratio capable of withstanding a lateral load at least 85% of the peak lateral load P_p. Table 2 gives the ultimate top displacement d_u and ultimate drift ratio θ_u of the four specimens. A ductility ratio μ was evaluated as the ratio of d_u to yield displacement d_y and presented in Table 2. Each specimen reached an ultimate drift ratio exceeding 1.8% and a ductility ratio greater than 2.7. Specimen DCW1 obtained the highest ultimate drift ratio even though this specimen also had the lowest ductility ratio. As shown in Fig. 7, the loss of lateral deformation capacity in any specimen was announced by steel tube fracture. In general, the deformation capacity decreased with increased aspect ratio. As stated previously, the steel tubes and faceplates buckled earlier in the slender walls DCW2 and DCW3 than in the squat wall DCW1. In addition, as described later, the strain at bottom of steel tubes increased more rapidly in DCW2 and DCW3 than in DCW1. These observations indicated that the steel tube of the walls with higher aspect ratios resisted greater axial force. Accordingly, DCW2 and DCW3 suffered earlier steel tube buckling and fracture. To achieve better lateral deformation capacity, stronger steel tubes may be needed in the proposed Co-DSC wall especially with a high aspect ratio. DCW3-R and DCW3 had similar lateral strength, while the drift at peak load of DCW3-R was 22% higher than that of DCW3. This indicated that the reinforcing sheaths delayed the peak load state without significantly increasing the base shear.

3.4 Energy Dissipation

The energy dissipated per loading cycle and the cumulative energy dissipation were evaluated for the specimens and shown in Fig. 8. In general, the squat specimen DCW1 had the lowest energy dissipation capacity. Specimens DCW2, DCW3, and DCW3-R similarly dissipated energy, indicating that both aspect ratio and the use of reinforcing sheaths caused negligible effect on energy dissipation for slender walls.

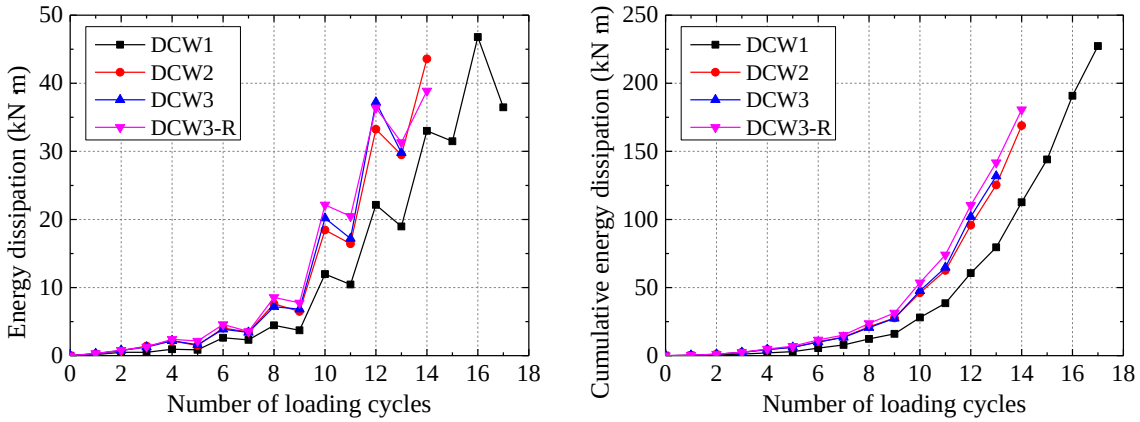

(a) Energy dissipation per loading cycle (b) Cumulative energy dissipation

Figure 8: Energy dissipation

4. Finite Element Modelling

The test results are analyzed using a nonlinear finite element (FE) program *ABAQUS*. Due to complexity of achieving numerical convergence, high nonlinearity in geometry and material, and steel-concrete interaction, Dynamic/Explicit was utilized to conduct nonlinear push-over analysis.

4.1 Material Constitutive Relationships

The material constitutive relationships of both concrete and steel are shown in Fig. 9. The concrete damage plasticity (CDP) model in *ABAQUS* was used as the constitutive model both for the concrete filled between the corrugated double steel faceplates, and the concrete filled in the steel tubes, denoted as unconfined concrete and confined concrete, respectively. The elastic-plastic model was used as the constitutive model for all steel parts in this FE model.

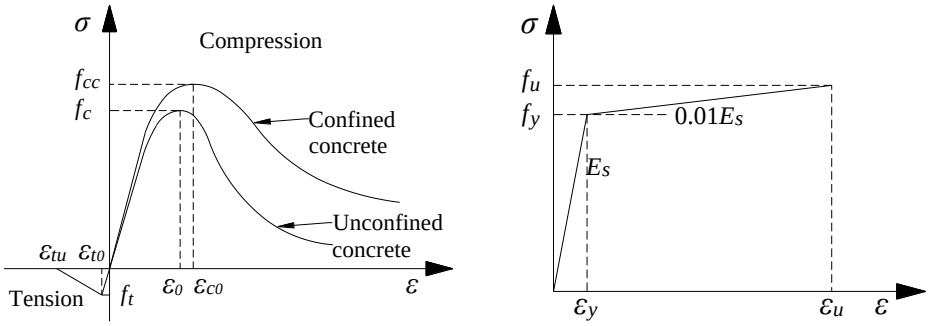

(a) Concrete (b) Steel

Figure 9: Material constitutive models

As shown in Eq. 2 to Eq. 5, the compressive stress-strain relationship of unconfined concrete can be obtained by using the method developed by Guo and Shi (2003).

$$x = \varepsilon/\varepsilon_c\,,\ y = \sigma/f_c \tag{2}$$

$$y = \begin{cases} \alpha_a x + (3-2\alpha_a)x^2 + (\alpha_a - 2)x^3 & (x<1) \\ \dfrac{x}{\alpha_d (x-1)^2 + x} & (x \geq 1) \end{cases} \tag{3}$$

$$\alpha_a = 2.4 - 0.0125\, f_c \tag{4}$$

$$\alpha_d = -0.905 + 0.157\, f_c^{0.785} \tag{5}$$

where f_c is the concrete compressive strength, ε_c is the compressive strain corresponding to f_c, α_a and α_d are the dimensionless parameters at the ascent and descent stages of uniaxial compressive stress-strain relationship of concrete, respectively.

The compressive stress-strain relationship of confined concrete developed by Han (2016) was adopted to simulate the compressive plastic damage behavior of the concrete filled in the steel tubes in this study. The compressive stress-strain relationship can be obtained from Eq. 6 to Eq. 13.

$$y = \begin{cases} 2x - x^2 & (x \le 1) \\ \dfrac{x}{\beta(x-1)^{\eta} + x} & (x > 1) \end{cases} \tag{6}$$

$$x = \varepsilon/\varepsilon_0,\ y = \sigma/\sigma_0 \tag{7}$$

$$\sigma_0 = [1 + (-0.0135\xi^2 + 0.1\xi)(24/f_c)^{0.45}]\, f_c \tag{8}$$

$$\xi = \frac{A_s f_y}{A_c f_c} \tag{9}$$

$$\varepsilon_0 = \varepsilon_{cc} + [1330 + 760(f_c/24 - 1)]\xi^{0.2} \quad (\mu\varepsilon) \tag{10}$$

$$\varepsilon_{cc} = 1300 + 12.5\, f_c \quad (\mu\varepsilon) \tag{11}$$

$$\eta = 1.6 + 1.5/x \tag{12}$$

$$\beta = \begin{cases} \dfrac{f_c^{0.1}}{1.35\sqrt{1+\xi}} & (\xi \le 3) \\ \dfrac{f_c^{0.1}}{1.35\sqrt{1+\xi}(\xi-2)^2} & (\xi > 3) \end{cases} \tag{13}$$

The tensile stress-strain relationship of concrete used in this study was obtained by using the method developed by Shen et al. (1993), which can be expressed as Eq. 14 to Eq. 17.

$$x = \varepsilon/\varepsilon_p,\ y = \sigma/\sigma_p \tag{14}$$

$$y = \begin{cases} 1.2x - 0.2x^6 & (x < 1) \\ \dfrac{x}{0.31\sigma_p^2(x-1)^{1.7} + x} & (x \ge 1) \end{cases} \tag{15}$$

$$\sigma_p = 0.26(1.25\, f_c)^{2/3} \tag{16}$$

$$\varepsilon_p = 43.1\sigma_p \quad (\mu\varepsilon) \tag{17}$$

where σ_p is the concrete tensile strength, and ε_p is the tensile strain corresponding to σ_p.

As shown in Eq. 18, the damaging evolution parameters of concrete in compression and tension were calculated using the method developed by Birtel and Mark (2006).

$$d_k = 1 - \frac{\sigma_k E_k^{-1}}{\varepsilon_k^{pl}\left(1/b_k - 1\right) + \sigma_k E_k^{-1}} \quad \left(k = t, c\right) \tag{18}$$

where d_k is the concrete damaging evolution parameters, σ_k is the concrete stress, E_k is the concrete Young's modulus, b_k is the ratio of plastic strain ε_k^{pl} to inelastic strain ε_k^{in}, t and c represent the concrete in tension and compression, respectively.

In order to improve the convergence and efficiency of the calculation, bi-linear plasticity model with Von-Mises yield surface, associated flow rule, and kinematic hardening was used for all steel elements, where true stress σ_{true}, true strain ε_{true} and plastic strain ε_{pl} can be obtained from Eq. 19 to Eq. 21.

$$\sigma_{true} = \sigma_{nom}\left(1 + \varepsilon_{nom}\right) \tag{19}$$

$$\varepsilon_{true} = \ln\left(1 + \varepsilon_{nom}\right) \tag{20}$$

$$\varepsilon_{pl} = \left|\varepsilon_{true}\right| - \left|\sigma_{true}\right| / E_s \tag{21}$$

where σ_{nom} and ε_{nom} are the nominal stress and strain, respectively, which can be obtained from the coupon test.

4.2 Elements, Loading, and Boundary Conditions

Eight-node solid elements with reduced integration (C3D8R) were used to simulate the infilled concrete, and four-node shell elements with reduced integration (S4R) were used to simulate the faceplates, steel tubes, and baseplates. Wire elements assigned by connector section properties, which would be explained later, were used to simulate the high strength tie bolts.

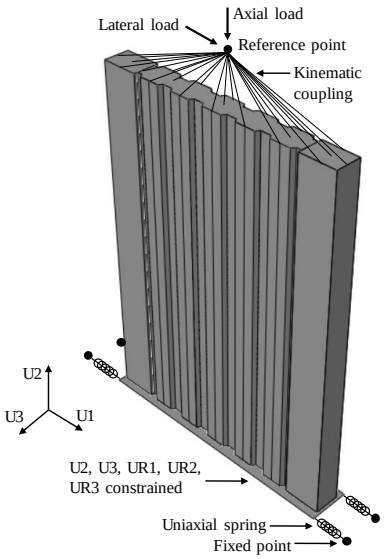

Figure 10: Schematic of FE model in *ABAQUS*

Fig. 10 shows the schematic of FE model in *ABAQUS*. The loading of the FE models was simulated by applying monotonic lateral displacements along U1 direction to a reference point (RP). RP located on the centroid axis of the specimen cross section, 150 mm above the top surface of the specimen, consisting with the height of the horizontal actuator in the test. Kinematic coupling interaction was defined to constrain the top surface of the specimen to RP in all translational and rotational freedoms.

The baseplate was used to simulate the foundation in the test. As is known, slight slippage of foundation is inevitable during the test, resulting in stiffness reduction of the specimen. Thus, the freedoms of U2, U3, UR1, UR2, and UR3 of baseplate were constrained, while the displacement of U1 was constrained by uniaxial spring elements with an axial stiffness calculated from the material and sectional properties of concrete filled steel box foundation beam in the test.

4.3 Contact and Connector Models

The algorithm General contact in *ABAQUS* was used to model the contact behavior between the steel and concrete. For this algorithm, tangential behavior was defined using penalty friction formulation with friction coefficient of 0.6, and normal behavior was defined using pressure-overclosure solution with hard contact properties.

The connector section of tie bolts was defined with a translational type of axial, and a rotational type of revolute, corresponding to the available freedoms of U3 and UR3, and the constrained freedoms of UR1 and UR2.

4.4 Validations of FE model

Fig. 11 shows comparisons of the lateral load-displacement responses simulated by the FE analyses with the envelope curves measured experimentally for specimens DCW1 to DCW3-R with aspect ratios of 1.0 to 2.0, respectively. The percentage error between tested peak load in positive direction P_T and the simulated peak load P_F was within 10% for all specimens. The initial stiffness simulated by the FE models were also in good agreement with the test values. These indicate that the FE analyses can reasonably simulate the overall behavior of the test specimens.

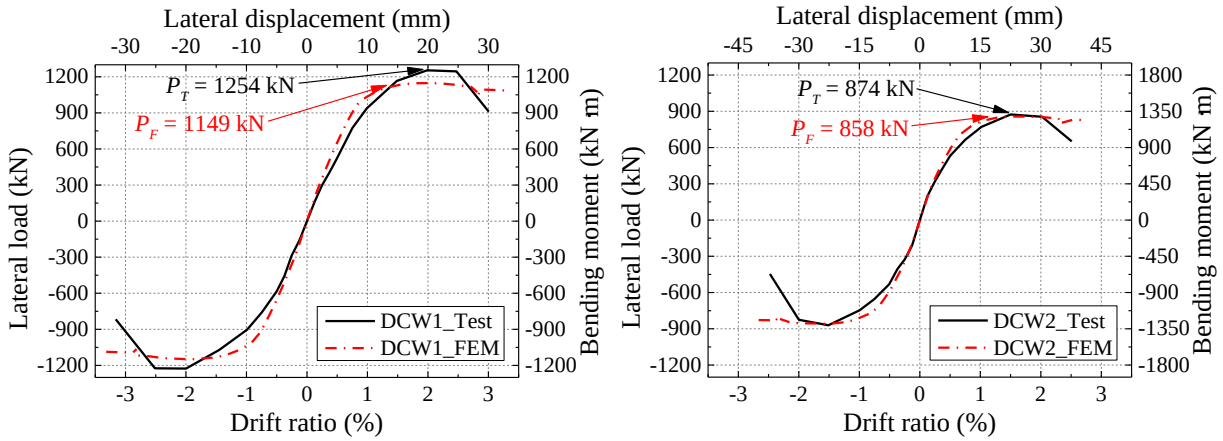

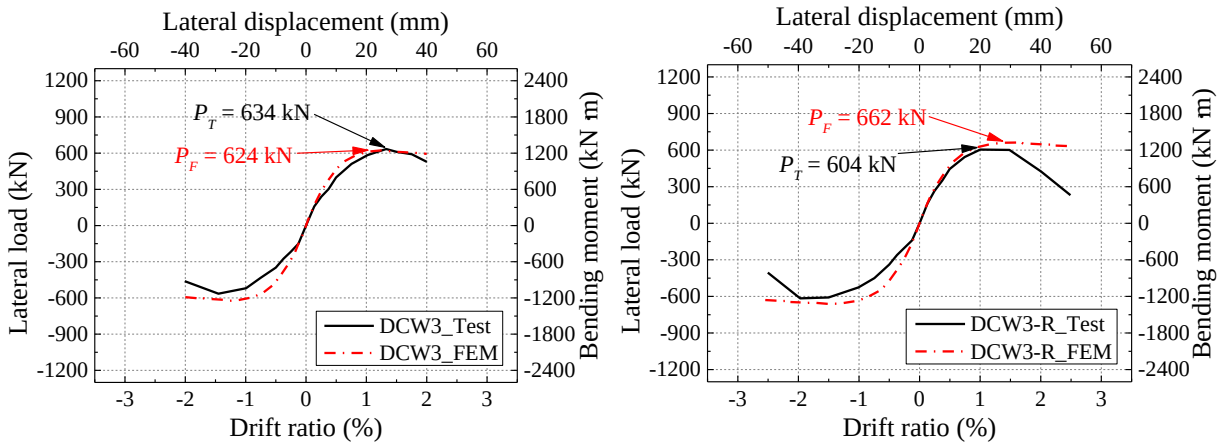

Figure 11: Comparison of experimental and analytical results

5. Parametric analysis

Based on the validated FE models, the effects of three primary parameters on lateral load-displacement relationship of Co-DSC walls were analyzed.

5.1 Aspect ratio

The FE models of Co-DSC walls with six aspect ratios of 0.5, 0.75, 1.0, 1.5, 2.0, and 2.5 were analyzed. Fig. 12 shows the effects of aspect ratio λ on lateral load-displacement relationship and Von-Mises stress development at 3.5% drift of Co-DSC walls. The lateral strength and stiffness of Co-DSC walls decreased with the increase of wall aspect ratio. The maximum Von-Mises stress of Co-DSC walls with aspect ratios no more than 1.0 distributed along the diagonal direction of the wall, while the maximum Von-Mises stress of Co-DSC walls with aspect ratios no less than 1.5 distributed horizontally at wall base, indicating typical compression-shear and compression-flexure failure patterns, respectively.

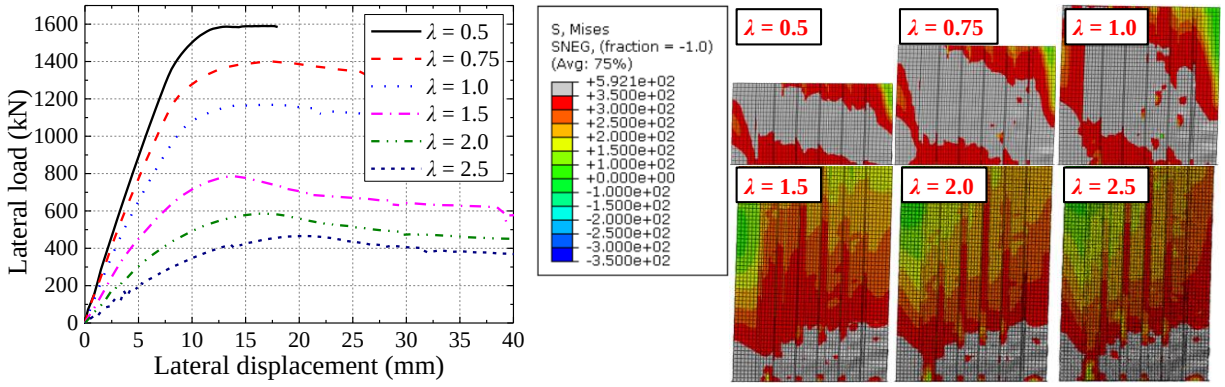

Figure 12: Effects of aspect ratio

5.2 Axial load ratio

Two groups of FE models, corresponding to compression-shear Co-DSC walls with aspect ratio of 0.75, and compression-flexure Co-DSC walls with aspect ratio of 2.0, were analyzed respectively. Fig. 13 shows the effects of axial load ratio *n* on lateral load-displacement relationship of Co-DSC walls. The lateral stiffness of Co-DSC walls increased with the increase of axial load ratio, while the deformation capacities were the opposite. The lateral strength

increased along with the axial load ratio before n = 0.2, and decreased after that. Because the failure of compression-flexure walls was primarily caused by wall base buckling and fracture in compression, axial load ratio had more significant effects on lateral load-displacement relationship of compression-flexure walls. In order to ensure the expected deformation capacity and ductility, an upper axial load ratio of 0.4 is recommended.

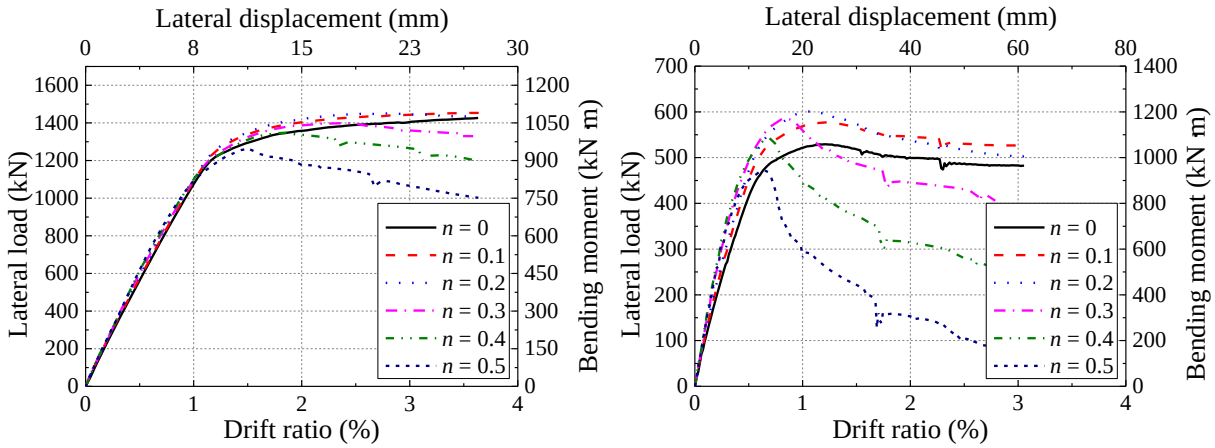

(a) Compression-shear dominated Co-DSC walls (b) Compression-flexure dominated Co-DSC walls

Figure 13: Effects of axial load ratio

5.3 Ratio of tie bolt spacing to faceplate thickness

Both the two groups of compression-shear Co-DSC wall and compression-flexure Co-DSC wall FE models with ratio of tie bolt spacing to faceplate thickness κ = 82, 58, 47, corresponding to 5, 4, and 3 corrugates, were analyzed. Fig. 14 shows the effects of ratio of tie bolt spacing to faceplate thickness κ on lateral load-displacement relationship. The ratio of tie bolt spacing to faceplate thickness had negligible effects on lateral stiffness of the walls, while had significant effects on lateral strength and deformation capacities of the walls. These were because that the faceplates with sparse tie bolts were prone to buckling at damage developing loading stage. However, the ratio of tie bolt spacing to faceplate thickness of FE model with the densest tie bolts of 47 exceeded the upper limit of that for flat faceplate of 37, indicating that using corrugated plate as faceplate contributed to reduce the number of tie bolts.

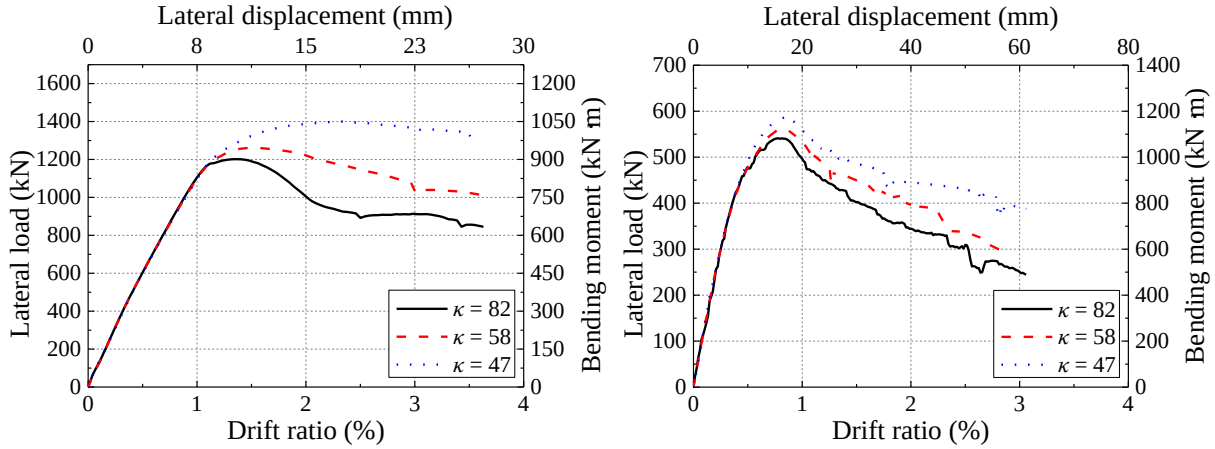

(a) Compression-shear dominated Co-DSC walls (b) Compression-flexure dominated Co-DSC walls

Figure 14: Effects of ratio of tie bolt spacing to faceplate thickness

6. Conclusions

A new type of earthquake-resistant composite structural wall, named Co-DSC wall, was experimentally and numerically studied. The Co-DSC wall consisted of concrete-filled steel tube boundary columns and corrugated double steel faceplates connected by tie bolts and infilled with plain concrete. Three 1/3-scale specimens with different aspect ratios and one additional specimen strengthened with reinforcing sheaths at steel tube bottom were tested under combined axial and cyclic lateral loading. Based on the FE model validation, primary parameters influencing the seismic performance of Co-DSC walls were analyzed. The following major conclusions were reached:

(1) The specimens presented desired seismic performance and reached an ultimate drift ratio exceeding 1.8% and a ductility ratio greater than 2.7. The specimens experienced similar damage progress. The steel tubes and the faceplates buckled prior to reaching the peak load. The fracture of steel tubes resulted in the ultimate failure. Using stronger steel tubes would improve the lateral deformation capacity, but note that it would also increase the base shear.

(2) FE models were conducted by *ABAQUS*. Both lateral strength and initial stiffness simulated by the FE models were in good agreement with the test results. The FE models described in this paper can reasonably simulate the overall behavior of the test specimens.

(3) The moment-carrying capacity of the Co-DSC wall was not affected by wall aspect ratio. The squat walls with aspect ratio no more than 1.0 presented compression-shear failure, and the slender walls with aspect ratio no less than 1.5 presented compression-flexure failure. The squat wall achieved higher drift capacity but dissipated less energy than the slender walls.

(4) An upper axial load ratio of 0.4 was recommended to ensure the expected deformation capacity and ductility. Using corrugated plate as faceplate contributed to reduce the number of tie bolts, which could significant improve the construction and economy efficiency.

(5) The use of reinforcing sheaths improved the drift at peak load to a certain extent without significantly increasing the base shear of the specimen. However, the reinforcing sheaths could not constrain the steel tube buckling at post-peak stage, presumably due to insufficient thickness of the reinforcing sheaths. To achieve better lateral deformation capacity, using thicker reinforcing sheaths is recommended for the proposed Co-DSC walls.

Acknowledgments

The presented work was sponsored by the National Natural Science Foundation of China (Grants Nos. 51378340, 51678406 and 51878447). The authors would like to express their sincere gratitude to the sponsors.

References

ABAQUS 6.13. [Computer software]. Dassault Systèmes Simulia, Providence, RI.

Birtel V., Mark P. (2006). "Parameterised finite element modelling of RC beam shear failure." *Proceedings of the 19th Annual International ABAQUS Users' Conference*, Boston, MA., 95-108.

Cao W., Yu C., Dong H., Qiao Q., Han L., and Zhang Y. (2013). "Experimental study on seismic performance of composite shear walls with double steel plates under different constructions." *Journal of Building Structures*, 34(S1), 186-191 (in Chinese).

Clubley S.K., Moy S.S.J., and Xiao R.Y. (2003). "Shear strength of steel-concrete-steel composite panels. Part I-testing and numerical modelling." *Journal of Constructional Steel Research*, 59, 781-794.

Epackachi S., Nguyen N.H., Kurt E.G., Whittaker A.S., and Varma A.H. (2015). "In-plane seismic behavior of rectangular steel-plate composite wall piers." *Journal of Structural Engineering*, 141(7), 04014176.

Guo Z., Shi X. (2003). *Reinforced concrete theory and analyse*, Tsinghua University Press, Beijing.

Han L. (2016). *Concrete filled steel tubular structures-theory and practice*, Science Press, Beijing.

Hossain K.M.A., and Wright H.D. (2004). "Experimental and theoretical behavior of composite walling under in-plane shear." *Journal of Constructional Steel Research*, 60(1), 59-83.

Hossain K.M.A., Rafiei S., Lachemi M., and Behdinan K. (2016). "Structural performance of profiled composite wall under in-plane cyclic loading." *Engineering Structures*, 110, 88-104.

Huang Z., and Liew J.Y.R. (2016). "Structural behaviour of steel-concrete-steel sandwich composite wall subjected to compression and end moment." *Thin-Walled Structures*, 98, 592-606.

Ji X., Jiang F., and Qian J. (2013). "Seismic behavior of steel tube-double steel plate-concrete composite walls: Experimental tests." *Journal of Constructional Steel Research*, 86, 17-30.

Ji X., Cheng X., Jia X., and Varma A.H. (2017). "Cyclic in-plane shear behavior of double-skin composite walls in high-rise buildings." *Journal of Structural Engineering*, 143(6), 04017025.

Liew J.Y.R., and Sohel K.M.A. (2009). "Lightweight steel-concrete-steel sandwich system with J-hook connectors." *Engineering Structures*, 31, 1166-1178.

Link R.A., and Elwi A.E. (1995). "Composite concrete-steel plate walls: Analysis and behavior." *Journal of Structural Engineering*, 121(2), 260-271.

Mckinley B., and Boswell L.F. (2002). "Behavior of double skin composite construction." *Journal of Constructional Steel Research*, 58, 1347-1359.

Nie J., Hu H., Fan J., Tao M., Li S., and Liu F. (2013). "Experimental study on seismic behavior of high-strength concrete-filled double-steel-plate composite walls." *Journal of Constructional Steel Research*, 88(9), 206-219.

Ovarlez G., and Roussel N. (2006). "A physical model for the prediction of lateral stress exerted by self-compacting concrete on formwork." *Materials and Structures*, 39(2), 269-279.

Ozaki M., Akita S., Osuga H., Nakayama T., and Adachi N. (2004). "Study on steel plate reinforced concrete panels subjected to cyclic in-plane shear." *Nuclear Engineering and Design*, 228, 225-244.

Qian J., Jiang Z., and Jiang F. (2012). "Behavior of steel tube-reinforced concrete composite walls subjected to high axial force and cyclic loading." *Engineering Structures*, 36, 173-184.

Rafiei S., Hossain K.M.A., Lachemi M., and Behdinan K. (2015). "Profiled sandwich composite wall with high performance concrete subjected to monotonic shear." *Journal of Constructional Steel Research*, 107, 124-136.

Rassouli B., Shafaei S., Ayazi A., and Farahbod F. (2016). "Experimental and numerical study on steel-concrete composite shear wall using light-weight concrete." *Journal of Constructional Steel Research*, 126, 117-128.

Seo J., Varma A.H., Sener K., and Ayhan D. (2016). "Steel-plate composite (SC) walls: In-plane shear behavior, database, and design." *Journal of Constructional Steel Research*, 119, 202-215.

Shanmugam N.E., Kumar G., and Thevendran V. (2002). "Finite element modelling of double skin composite slabs." *Finite Elements in Analysis and Design*, 38, 579-599.

Shen J., Wang C., Jiang J. (1993). *Reinforced concrete finite element analyse and shell element limit state analyse*, Tsinghua University Press, Beijing.

Stephens M.J., and Zimmerman T.J.E. (1990). "The strength of composite ice-resisting walls subjected to combined loads." *Proceedings of 1st European Offshore Mechanics Symposium (EUROMS-90)*, Golden, Colo.

Tran T.A., and Wallace J.W. (2015). "Cyclic testing of moderate-aspect-ratio reinforced concrete structural walls." *ACI Structural Journal*, 112(6), 653-665.

Wright H.D. (1995). "Local stability of filled and encased steel sections." *Journal of Structural Engineering*, 121(10), 1382-1388.

Wright H.D., and Gallocher S.C. (1995). "The behavior of composite walling under construction and service loading." *Journal of Constructional Steel Research*, 35(3), 257-273.